Rashba-like Spin Textures in Graphene Promoted by Ferromagnet-Mediated Electronic Hybridization with a Heavy Metal

Beatriz Muñiz Cano, Adrián Gudín, Jaime Sánchez-Barriga, Oliver Clark, Alberto Anadón, Jose Manuel Díez, Pablo Olleros-Rodríguez, Fernando Ajejas, Iciar Arnay, Matteo Jugovac, Julien Rault, Patrick Le Fèvre, François Bertran, Donya Mazhjoo, Gustav Bihlmayer, Oliver Rader, Stefan Blügel, Rodolfo Miranda, Julio Camarero, Miguel Angel Valbuena, and Paolo Perna

Rashba-like spin textures in graphene promoted by ferromagnet-mediated electronic hybridization with a heavy metal

Beatriz Muñiz Cano,[1,†] Adrián Gudín,[1,2,†] Jaime Sánchez-Barriga,[1,3] Oliver Clark,[3] Alberto Anadón,[1] Jose Manuel Díez,[1,2] Pablo Olleros-Rodríguez,[1] Fernando Ajejas,[1] Iciar Arnay,[1] Matteo Jugovac,[4] Julien Rault,[5] Patrick Le Fèvre,[5] François Bertran,[5] Donya Mazhjoo,[6] Gustav Bihlmayer,[6] Oliver Rader,[3] Stefan Blügel,[6] Rodolfo Miranda,[1,2] Julio Camarero,[1,2] Miguel Angel Valbuena,[1,*] and Paolo Perna[1,*]

[1]*IMDEA Nanoscience, C/ Faraday 9, Campus de Cantoblanco, 28049 Madrid, Spain*
[2]*Departamento de Física de la Materia Condensada, Instituto Nicolás Cabrera and Condensed Matter Physics Center (IFIMAC), Universidad Autónoma de Madrid, Campus de Cantoblanco, 28049 Madrid, Spain*
[3]*Helmholtz-Zentrum Berlin für Materialien und Energie, Albert-Einstein-Str. 15, 12489 Berlin, Germany*
[4]*Elettra Sincrotrone Trieste, Strada Statale 14 km 163.5, 34149 Trieste, Italy*
[5]*Synchrotron SOLEIL, Saint-Aubin, 91192 Gif-sur-Yvette, France*
[6]*Peter Grünberg Institute and Institute for Advanced Simulation, Forschungszentrum Jülich, D-52425 Jülich, Germany*

Abstract

Epitaxial graphene/ferromagnetic metal (Gr/FM) heterostructures deposited onto heavy metals have been proposed for the realization of spintronic devices because of their perpendicular magnetic anisotropy and sizeable Dzyaloshinskii-Moriya interaction (DMI), allowing for both enhanced thermal stability and stabilization of chiral spin textures. However, establishing routes towards this goal requires the fundamental understanding of the microscopic origin of their unusual properties. Here, we elucidate the nature of the induced spin-orbit coupling (SOC) at Gr/Co interfaces on Ir. Through spin- and angle-resolved photoemission spectroscopy along with density functional theory, we show that the interaction of the heavy metals with the Gr layer via hybridization with the FM is the source of strong SOC in the Gr layer. Furthermore, our studies on ultrathin Co films underneath Gr reveal an energy splitting of ~ 100 meV for in-plane and negligible for out-of-plane spin polarized Gr π bands, consistent with a Rashba-SOC at the Gr/Co interface, which is either the fingerprint or the origin of the DMI. This mechanism vanishes at large Co thicknesses, where neither in-plane nor out-of-plane spin-orbit splitting is observed, indicating that Gr π states are electronically decoupled from the heavy metal. The present findings are important for future applications of Gr-based heterostructures in spintronic devices.

Keywords: graphene, cobalt intercalation, spin-orbit coupling, Rashba effect, SR-ARPES, DFT, spintronics.

Introduction

Spintronics aims at exploiting the spin degree of freedom of electrons for new forms of information storage and logic devices [1]. A major challenge for innovative, high-speed, low-power operation spintronic devices is to develop suitable spin transport channels with long spin lifetime and propagation length. Graphene (Gr) is an ideal spin channel material, exhibiting the longest spin relaxation length ever measured at room temperature, of several micrometers [2–7], as well as enhanced spin-to-charge conversion and spin Hall effect when interfaced with heavier atoms [8, 9] due to spin-orbit coupling (SOC) [10].

While this interaction can drive to a modification of spin relaxation or spin diffusion lengths, strong SOC also dictates a vast variety of related intriguing phenomena, especially for reduced dimensions. Prominent examples are the quantum spin Hall (QSH) and anomalous Hall (QAH) states [11–17], as well as the interfacial Rashba effect and the Dzyaloshinskii-Moriya interaction (DMI) [18, 19]. In relation to the latter, as the interplay between Rashba textures and the DMI is rooted in their common origin in a strong SOC and the absence of inversion symmetry, the first can promote or strengthen the second [20, 21], thereby stabilizing chiral spin textures. Such a connection gives rise to non-trivial magnetic states, including the emergence of skyrmions [22, 23] enabling the development of efficient non-volatile storage technologies [24–27].

However, Gr is a material of negligible SOC in its pristine state. At the $\overline{\mathrm{K}}$ point of the Gr surface Brillouin zone (SBZ), where the Dirac point (DP) is located at the Fermi level (E_F), the SOC-induced gap is very small, of only 24-50 μeV [28]. To observe spin-orbit effects suitable for applications, it is thus necessary to enhance the SOC in Gr while preserving its Dirac cone structure. The required high nuclear charge can in principle be achieved by combining Gr with appropriate substrates [29–32], or by intercalation of heavy atoms in suitable geometries [33–37], resulting in a strong hybridization and a spin splitting which can be deliberately induced in the vicinity of the DP. For instance, Au intercalation at the Gr/Ni interface has been demonstrated to create a giant spin-orbit splitting (~ 100 meV) of the Gr Dirac cone up to the Fermi energy [33] due to an in-plane Rashba spin polarization caused by hybridization with Au states. A Rashba splitting of ~ 100 meV was also measured for Gr/Au/SiC [38]. Besides, in the case of Gr/Pb bilayers grown on Pt(111) [35, 39], the observed enhancement of SOC has been explained in terms of intrinsic (Kane and Mele [11]) and extrinsic (Rashba [34]) SOC contributions, responsible for out-of-plane and in-plane spin polarizations, respectively.

In the context of magnetic properties, the intercalation of thin ferromagnetic metal (FM) layers underneath Gr is considered a promising approach for developing multifunctional devices as it enables control of the spin filtering and injection efficiency [40–42], exchange coupling [43], tunnel magnetoresistance [44], Rashba effect [34, 45–48], topological electronic flattened bands [49] and perpendicular magnetic anisotropy (PMA) [20, 50–54], as well as the stabilization of magnetic skyrmions [55, 56]. The combination of spin-orbit interaction and ferromagnetism offers exciting possibilities for electrical control of topologically-protected chiral spin textures in Gr/FM heterostructures, where an unexpectedly large interfacial DMI has been observed to play a key role [20, 53]. However, this raises questions about how Gr can induce a large interfacial DMI where SOC is weak. While the strong hybridization between Gr and FM states [57–60] has been previously identified as one of the key ingredients underlying the enhancement of interfacial PMA [51, 52], direct spectroscopic evidence of the exact microscopic mechanism that is ultimately responsible for the significant increase of DMI at Gr/FM interfaces remains elusive.

Earlier on, it has been suggested that Gr plays an essential role in determining the unusual properties of Gr/FM interfaces in the absence of strong SOC. For instance, on the one hand, in the case of Gr/Co interfaces, it has been experimentally found that the hybridization of Co $3d$ orbitals with Gr bands can lead to an enhancement of the interfacial PMA [51, 52] via the anisotropy of the orbital magnetic moments [51]. On the other hand, based on density functional theory (DFT) calculations of the electronic structure of Gr/Co bilayers on Ru(0001), the physical origin of the DMI at Gr/Co interfaces has been attributed to a Rashba effect originating from large variations of the SOC energy in the Co layer [20]. These variations have been explained by the strong influence that the change in the potential gradient induced by Gr at the interface has on the Co $3d$ orbitals [20, 53]. However, in this case, a Rashba splitting as small as 1.28 meV is predicted to be the reason for a considerable enhancement of the effective SOC value at the interface [20]. This is in contrast to the case of Co/Pt interfaces, where the DMI has been explained by a Fert-Levy model [61, 62], according to which the DMI at the vacuum/FM interface should scale with the SOC in the material that is on the non-magnetic side of the interface underneath the FM layer. Conversely, very recent DFT calculations revealed that the DMI at both Gr/Co and Co/Pt interfaces may have a common physical origin, with the effect of Gr being to reduce the total DMI of the hererostructure by the inversion of the chirality of the vacuum/Co interfacial DMI [63].

To address these issues, we experimentally investigate the electronic origin of the large DMI at Gr/FM interfaces. To this end, we use angle-resolved photoemission (ARPES) with and without spin resolution to systematically characterize the electronic structure of high quality Gr-based heterostructures with atomically flat interfaces and a homogeneous intercalated Co layer sandwiched between Gr and an epitaxial Ir(111) layer. Unlike previous studies in which Gr/FM interfaces of high quality were only grown on metallic single-crystal substrates, our heterostructures consist of interfaces of the same excellent quality grown on insulating commercial oxide substrates, which enable their suitability for real spintronic devices in which injected currents (electrical or spin) are not drained by the substrate [51, 53, 64, 65]. Our main finding is that a strong SOC induced in the Gr layer underlies the significant enhancement of the interfacial DMI. The effect manifests itself by a spin splitting of Gr π-states which is consistent with a Rashba-SOC at the Gr/Co interface two orders of magnitude larger than what was previously assumed. The experimental results are supported by DFT calculations, pinpointing the interaction between Gr and the heavy metal layer via the FM as the main source of SOC for Gr. Our findings hold significant implications for the integration of Gr-based heterostructures into technologies with advanced functionalities for next-generation spintronic devices.

Results and discussion

Electronic properties of pristine and Co-intercalated Gr/Ir

In order to understand the importance of the hybridization effects involving Gr π-states for the enhancement of SOC at the interface, ARPES measurements of the electronic structure before and after systematic Co intercalation were performed at first. The procedure adopted for the preparation of epitaxial Gr-based heterostructures is described in more detail in the Methods section and extensively reviewed in ref. [64]. In brief, a 30-nm-thick Ir buffer was DC sputtered at 670 K on an insulating Al_2O_3(0001) substrate, onto which epitaxial Gr was subsequently grown by ethylene dissociation at 1025 K. After Gr growth, Co was deposited by electron-beam evaporation at room temperature and its intercalation under Gr was promoted by a moderate thermal annealing, previously calibrated to ensure complete intercalation and avoid Co-Ir alloying effects [64]. The high quality of the interfaces and the completion of the intercalation process were checked by ARPES and low-energy electron diffraction (LEED) (see Figs. 1 and 2).

The energy-momentum band dispersion of Gr/Ir/Al_2O_3 (0001) measured by ARPES along the $\overline{\Gamma}$-$\overline{K}$-$\overline{M}$ direction of the Gr SBZ is presented in Figs. 1(a)-(c). The overall electronic structure is consistent with the characteristic quasi-freestanding character of the Gr layer on Ir(111), and comparable to the case of Gr grown on Ir(111) single-crystal substrates [37, 66–68], proving the high quality of the Gr/Ir interface. The photoemission features of the Gr σ and π bands are very sharp and intense, as evidenced by the momentum-distribution curve (MDC) at an energy of $E\text{-}E_F = -150$ meV and the energy-distribution curve (EDC) at the $\overline{K}$ point of the Gr SBZ (Figs. 1(d) and (e), respectively), confirming again the interface quality. The dominant feature in the spectrum is the Gr π band, whose bottom is located at $\overline{\Gamma}$, at an energy of $E\text{-}E_F \approx -8.28$ eV, and disperses linearly towards E_F resulting in the formation of a slightly n-doped Dirac cone, as inferred from the MDC and EDC analyses. The narrowest MDC cor-

responding to an energy of -150 meV (DP energy) can be fit to a Lorentzian function, whose full width at half maximum (FWHM) is ≈ 0.0061 Å^{-1}, similar to the FWHM value obtained for Gr grown on Ir(111) single-crystal substrates [67]. In the band dispersion, Gr π band replicas expected due to the additional periodicity of the moiré lattice can be distinguished (see, e.g. Fig. 1(d)) despite their much lower intensity when compared to the main Gr Dirac cone.

These Dirac cones are also visible at the Fermi surface (FS) and constant energy (CE) maps in Fig. 1(f). Here, the main Dirac cones at the $\overline{\text{K}}$ and $\overline{\text{K}}'$ points, whose dispersions are indicated by red dashed lines, exhibit the characteristic trigonal symmetry of quasi-freestanding Gr on Ir(111), and coexist with the band dispersion of Ir 5d states typically observed in Ir(111) bulk single crystals (the ellipsoidal-shaped features close to E_F [59, 69]). The Gr and Ir SBZs, indicated by red and orange hexagons in Fig. 1(f), can also be clearly identified from the intensity of the CE contours associated with the different features. Additionally, hybridization between Ir 5d and Gr π states can be observed in the energy region between -1 and -4 eV, leading to a reduction of the spectral weight at the band crossings along the $\overline{\Gamma}$-$\overline{\text{K}}$ direction, as seen in Fig. 1(a). Nonetheless, hybridization effects are rather weak so that the overall quasi-relativistic Dirac-like dispersion is largely preserved as in the case of weakly bonded systems, where the electronic structure is usually similar to that of freestanding Gr [58].

In Fig. 2 and Fig. S1 of the Supporting Information (Supp. Info.), an overview of the electronic band structure is provided, as seen by ARPES along the $\overline{\Gamma}$-$\overline{\text{M}}$-$\overline{\text{K}}$-$\overline{\Gamma}$ direction before (Fig. 2(a)) and after intercalation of an epitaxial Co film of 2 and 10 monolayers (ML) thickness (Fig. 2(b) and (c), respectively). The LEED images in Fig. 2(a) and (b) are consistent with the well-known $\sim 10\times10$ moiré pattern due to the coexistence of the incommensurate unit cells of Ir and Gr [51, 64, 70]. In contrast, a clear commensurate Gr structure can be observed in Fig. 2(c) decoupling the Gr layer from the Ir substrate. The overall energy-momentum dispersion of Gr π and σ states in the pristine Gr/Ir/Al_2O_3(0001) sample (Fig. 2(a)) is observed to be comparatively close to that of a weakly interacting layer system. The dispersing Ir-derived bands between -4 eV and E_F, mainly consisting of the two concentrical ellipsoidal pockets centered at the $\overline{\text{M}}_{\text{Ir}}$ point of the Ir SBZ [59, 69], and the Rashba-split Ir surface state (SS) dispersing towards $\overline{\Gamma}$ [71], can be distinguished.

Upon Co intercalation, the overall electronic band structure of Gr, as compared to Gr/Ir/Al_2O_3(0001), becomes strongly modified because the Gr-Co interaction is stronger than the Gr-Ir interaction. As a result, the Gr π band for a 2-ML-thick intercalated Co film is significantly downshifted in energy by $\sim$2 eV, as seen in Fig. 2(b) and Figs. S1 and S2 in Supp. Info. Specifically, the bottom of the π band at the $\overline{\Gamma}$ point is shifted from -8.28 to -10.08 eV, and the Dirac cone merges with the Co 3d states at $\sim$-2.80 eV in the vicinity of the $\overline{\text{K}}$ point. Further Co intercalation (10 ML) results in a double π band dispersion, as seen in the ARPES maps of

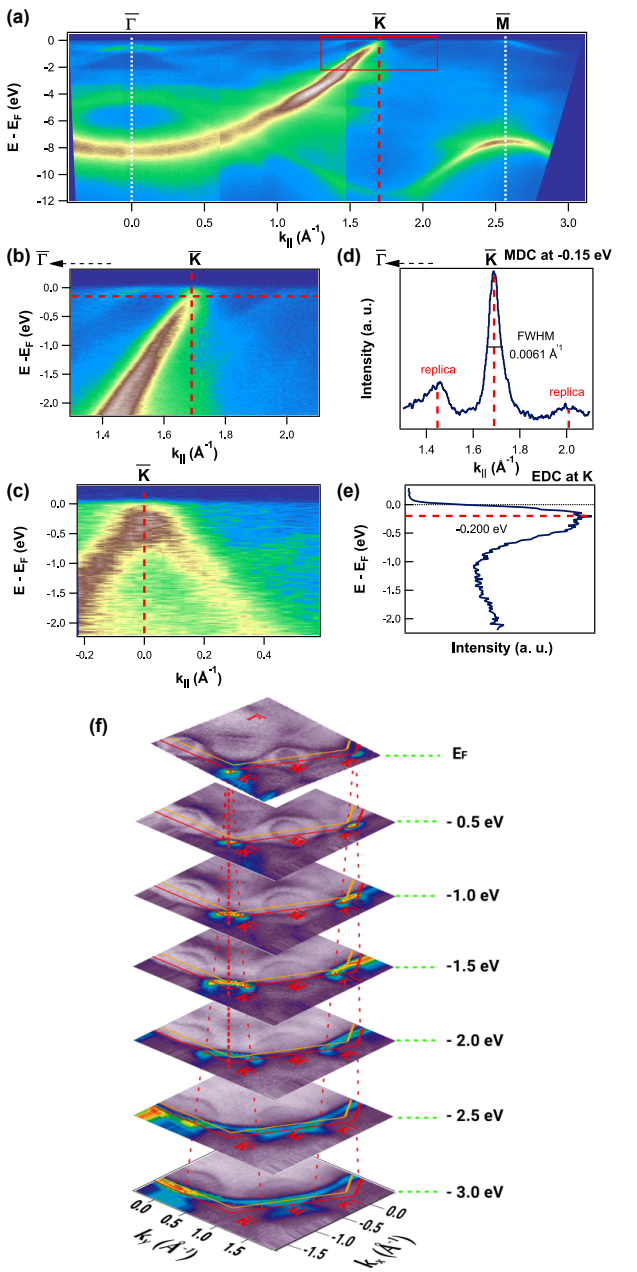

FIG. 1. **Electronic structure of Gr/Ir/Al_2O_3(0001)**. ARPES intensity band map along the $\overline{\Gamma}$-$\overline{\text{K}}$-$\overline{\text{M}}$ direction. (b) Zoom-in over the region of the Dirac cone corresponding to the red rectangle in (a). (c) Perpendicular cut to the $\overline{\Gamma}$-$\overline{\text{K}}$ direction centered at the $\overline{\text{K}}$ point. (d) MDC and (e) EDC profiles extracted at the energy and momentum positions indicated in (b) and (c). (f) FS and CE maps. Red dashed vertical lines indicate the Gr Dirac cones at $\overline{\text{K}}$ and $\overline{\text{K}}'$. Ir and Gr SBZs are indicated by orange and red hexagons, respectively.

Fig. 2(c) and in the EDC profiles in Fig. S2 (Supp. Info.), extracted at the momentum positions indicated by green dashed lines in Fig. 2. The double π band feature can be interpreted as a nearly-undisturbed Gr/Ir π band closer to E_F plus the more electronically doped π' Gr/Co band at higher binding energies, associated with a highly-interacting, commensurate

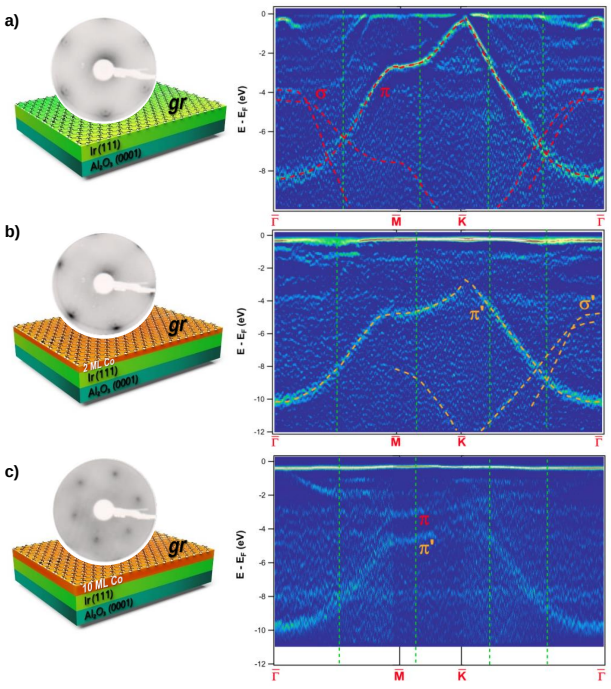

FIG. 2. **Characterization of Co-intercalated Gr/Ir/Al_2O_3(0001) heterostructures**. Evolution of the electronic properties. (a)-(c) LEED images and curvature ARPES band maps. The band dispersions provide an overview of the electronic structure of (a) Gr/Ir and Co-intercalated, (b) Gr /2 ML Co /Ir and (c) Gr /10 ML Co /Ir systems along the $\overline{\Gamma}$-$\overline{M}$-$\overline{K}$-$\overline{\Gamma}$ direction. Red and orange dashed lines follow the Gr π and σ bands for Gr/Ir and Gr /2 ML Co /Ir/, respectively. On the left, the schematic sketches of the corresponding heterostructures and their LEED patterns acquired at energies of (a), (b) 69 eV and (c) 155 eV are shown. Note that the ARPES band maps were obtained after applying the curvature algorithm of Ref. 72 in order to obtain sharper and better resolved electronic band dispersions (raw data shown in Fig. S1 in Supp. Info.). Green dashed vertical lines in the ARPES band maps indicate the positions at which the EDC profiles shown in Fig. S2 in Supp. Info. have been extracted.

phase. As reported earlier [51], the intercalation of further Co layers leads to a relaxation of the Co lattice resulting in a strong corrugation of the Gr layer. Although the intercalation of Co underneath Gr is layer-by-layer and epitaxial [51], the formation of Co clusters or inhomogeneities at large thicknesses cannot be completely ruled out and can eventually lead to a more corrugated Gr layer [51, 58]. The double π band dispersion can thus be associated to a corrugated Gr layer where the π band feature appears due to weakly interacting, hill, Gr atoms, while the π' band arises from highly interacting, valley, Gr atoms, in qualitative agreement with previous findings on other intercalated systems [58].

Moreover, several prominent Co electronic states can be identified in Figs. 2(b) and (c): (i) a narrow and very intense Co peak close to E_F, present along the entire $\overline{\Gamma}$-$\overline{M}$-$\overline{K}$-$\overline{\Gamma}$ direction in an energy range between -0.2 and -0.5 eV, and common to the two studied Co thicknesses; (ii) for the thicker (10 ML) Co system (Fig. 2(c)), a non-dispersing and broad state located at an energy of -8.0 eV is present in the band structure, which could be indicative of a more disordered thicker, though epitaxial, Co layer; (iii) another Co-derived band strongly dispersing from -1.9 eV to E_F towards $\overline{\Gamma}$, which confirms that, aside from the possible disorder, the intercalation of the thickest Co layer is mainly epitaxial; (iv) while Ir features can be distinguished only for the pristine and the 2 ML Co-intercalated Gr/Ir/Al_2O_3(0001) system, they disappear as the Co thickness is increased (i.e. 10 ML Co).

Now we will show for the 2 ML Co system that Co states hybridize with Ir states. We use the $\overline{\Gamma}$-$\overline{M}$ direction where there are no Gr states between -2.5 eV and E_F. Previous ARPES measurements have shown how after intercalation of one or more Co layers, the Ir bands close to E_F can barely be distinguished, while the Co 3d states are so intense and broad that the Ir 5d bands become blurred and diffuse [58, 59]. A zoom-in on the electronic structure from E_F to -5.5 eV for both Gr/Ir/Al_2O_3(0001) and the intercalated Gr/2 ML Co/Ir/Al_2O_3(0001) systems along the $\overline{\Gamma}$-$\overline{M}$ and $\overline{\Gamma}$-$\overline{K}$ directions is shown in Fig. 3 and Fig. S3 (Supp. Info.), respectively. Raw and curvature ARPES band maps are displayed for both systems. The FS and CE maps are also presented in Figs. 4(a) and 4(b), as well as in Fig. S4 in the Supp. Info. First, it should be noted that, contrary to previous studies, different bands corresponding to the electronic states of the underlying Ir(111) layer can always be detected. Noticeably, the electronic states that make up the ellipsoidal electron pockets centered at $\overline{M}_{Ir}$ observed in the pristine structure in Fig. 4(a) are also unambiguously resolved for the Gr/2 ML Co/Ir/Al_2O_3 (0001) at the FS (Fig. 4(b)). The prominent Ir-derived band dispersing from -3.8 eV at 0.6 $Å^{-1}$ to E_F at 1.13 $Å^{-1}$ along the $\overline{\Gamma}$-$\overline{M}$ direction in Fig. 3(b) coincides with the same band for the Gr/Ir/Al_2O_3 (0001) system in Fig. 3(a). In this regard, hybridization between Co 3d states at approximately -0.5 and -1.2 eV (clearly resolved between 0.5 and 0.8 $Å^{-1}$ along the $\overline{\Gamma}$-$\overline{M}$ direction) and the Ir dispersing band becomes evident, as reflected in the regions of increased intensity (red arrows on raw ARPES band maps in Fig. 3(b)), and by the gap opening observed in both raw and curvature, ARPES band maps (blue dashed lines in Fig. 3(b)). The main gap opening of Ir dispersing band occurs between -1.1 and -0.65 eV at 0.99 $Å^{-1}$ along the $\overline{\Gamma}$-$\overline{M}$ direction (magnified in the inset in Fig. 3(b)). Such a hybridization is also reflected in the CE maps at -0.5 and -1.0 eV in Figs. 4(a) and (b), where the Ir ellipsoidal pockets near E_F in Gr/Ir/Al_2O_3(0001) (Fig. 4(a)) become closed ellipses when interacting with Co 3d states (Fig. 4(b)).

It is also important to note that, besides the Co-Ir hybridization close to $\overline{M}_{Ir}$; the Rashba-split Ir SS [71], with negative effective mass and maximum intensity at -0.26 eV at $\overline{\Gamma}$, is still visible after Co intercalation (albeit slightly modified by the interaction with Co 3d states), as can be inferred from the band maps along both $\overline{\Gamma}$-$\overline{M}$ (Fig. 3) and $\overline{\Gamma}$-$\overline{K}$ (Fig. S3 in Supp. Info.) directions. Because they are visible and shifted, we conclude that the Rashba-split Ir SS at $\overline{\Gamma}$ and Ir 5d bands close to $\overline{M}_{Ir}$ are preserved and hybridized after intercalation of 2 ML Co. Alloying effects between Co and Ir may occur at Co-Ir interfaces

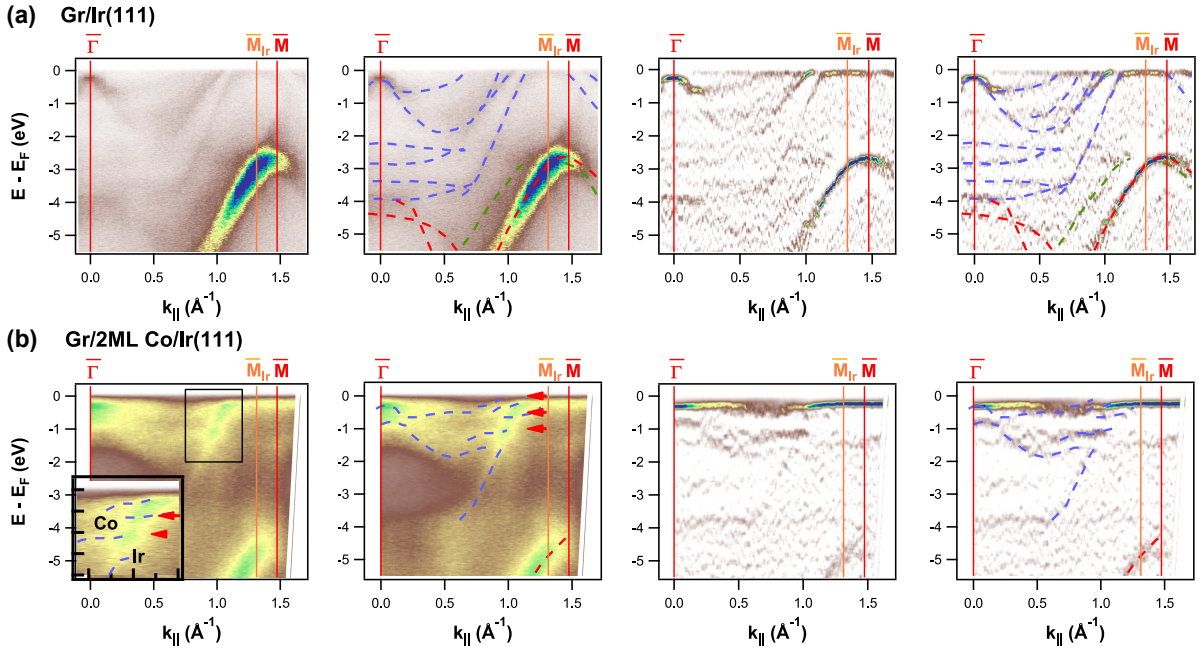

FIG. 3. **Hybridization effects between Co and Ir.** Zoom-in on the dispersion of the bands over the region close to E_F for (a) Gr/Ir/Al_2O_3(0001) and (b) Gr /2 ML Co /Ir/Al_2O_3(0001) heterostructures along the $\overline{\Gamma}$-$\overline{M}$ direction. Raw and curvature ARPES band maps with and without superimposed guidelines are presented, respectively. Blue dashed lines indicate the Ir-derived bands (a), which persist and hybridize with Co states (b), as evidenced by the corresponding gap openings. A close view of the gap regions is shown as an inset on the left panel in (b). Red and green dashed lines follow the Gr bands and a Gr replica originating from the moiré superlattice, respectively. Red arrows indicate the energies at which the CE contours shown in Fig. 4 have been obtained.

for lower coverages ($<$ 1 ML) and higher annealing temperatures. The formation of alloys could potentially lead to the recovery of the Dirac cone up to the Fermi level [73]. However, considering the soft thermal annealing process used for intercalation [64], the thickness of Co, and the observed electronic structure, these effects can be neglected in the samples studied here.

Another significant feature of the electronic structure of the 2 ML Co system is the development of mini Dirac cones in a narrow energy region of $\sim$0.2 eV below E_F at the $\overline{K}$ point (Fig. 4(c)). These mini Dirac cones have been previously observed in a perfectly oriented Gr layer on a Co(0001) surface and they strongly depend on the epitaxial quality of the interface [57]. The mini Dirac cones are due to the interaction of C $2p_z$ and Co $3d$ orbitals, have a fully two-dimensional character with their wave functions located at the interface, and are spin polarized. The development of the mini Dirac cone is a hallmark of the Co-Gr interaction, and the optimal interface [57].

To summarize this part, following intercalation of 2 ML Co, the Ir SS and Ir $5d$ bands are preserved in the vicinity of E_F, and become strongly modified due to the interaction with Co $3d$states. Moreover, the perfectly oriented epitaxial Gr layer leads to the formation of the mini Dirac cone as a result of the Co-Gr interaction. As observed in the electronic structure, further Co intercalation (i.e., $\geq$ 10 ML) decouples the Ir layer from the Gr/Co interface, eventually introducing some disorder effects. These results provide direct spectroscopic evidence of the Co-Ir electronic hybridization, including the Rashba-split Ir SS, as well as the Co-Gr electronic interaction. These findings indicate that there is the possibility that the spin-orbit interaction from the Ir layer is the main source of SOC a the Gr/Co interface.

Large Rashba-type spin-orbit splitting of Gr π states at the Gr/Co interface

In order to investigate whether a spin-orbit induced spin splitting is generated in Gr π states by Co intercalation, spin-resolved ARPES measurements were performed at selected wave vectors k of the Gr SBZ (Fig. 5(a)).

The spin-resolved EDCs for Gr /2 ML Co /Ir /Al_2O_3(0001) are presented in Figs. 5(b) and (c) (in-plane chiral and out-of-plane spin components, respectively), measured at 1.48 $Å^{-1}$ along the $\overline{\Gamma}$-$\overline{K}$ direction, as indicated by the dashed vertical line in the ARPES band map of Fig. 5(a), which crosses the region of the doped main Dirac cone with a stronger Gr character. To isolate and extract the precise contribution from the Gr π band in each spin channel separately, the spin-resolved EDCs in Fig. 5 were normalized and fit using five different components, which correspond to: Two peaks close to E_F arising from Co $3d$ states (turquoise color in Figs. 5(b) and 5(c)); the Gr σ band contribution (purple); a wide feature appearing after Co intercalation (grey, almost negligible contribution from disordered or localized states); and the intense contribu-

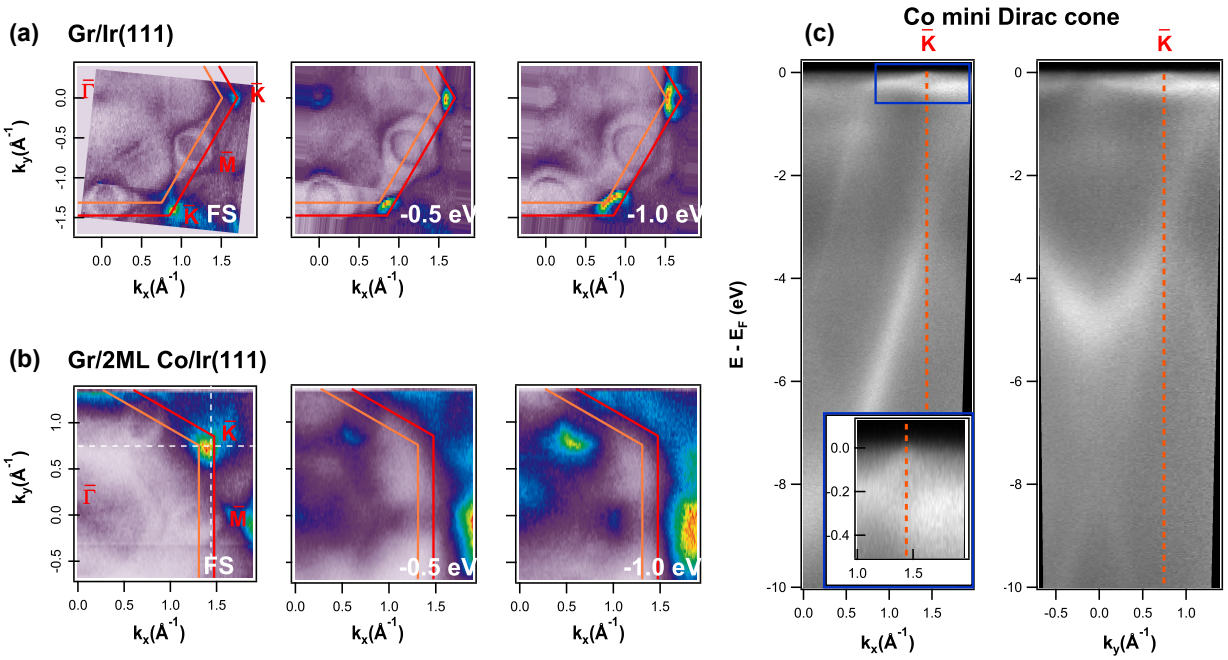

FIG. 4. **Observation of Co mini Dirac cones at the Gr/Co interface.** Fermi surface and constant energy contours acquired at energies of -0.5 and -1.0 eV for (a) Gr/Ir/Al_2O_3(0001) and (b) Gr /2 ML Co /Ir/Al_2O_3(0001) heterostructures. In each panel, the Gr and Ir hexagonal SBZs are indicated by red and orange solid lines, respectively. (c) Development of mini Dirac cones following Co intercalation. The band dispersions were taken along the two orthogonal momentum directions indicated by the white dashed lines crossing at $\overline{K}$ point in (b). On the left, a zoom-in over the region of the mini Dirac cone corresponding to the blue rectangular area near E_F is shown as an inset.

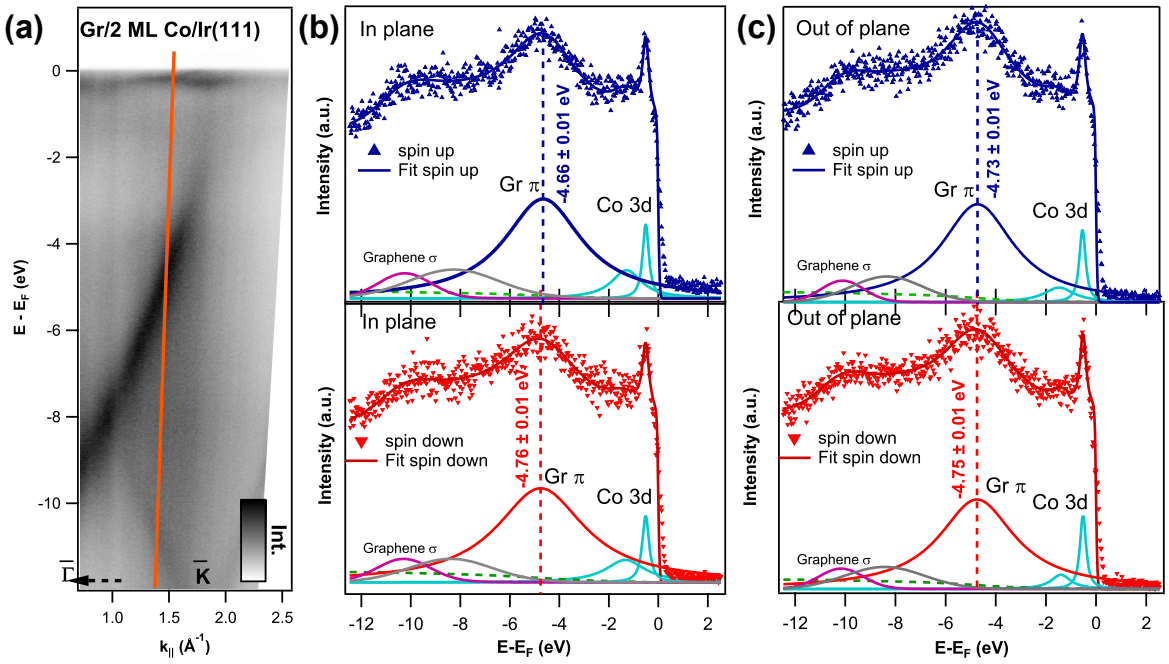

FIG. 5. **Rashba effect on Gr π states for 2 ML Co.** (a) Spin-integrated band dispersion of Gr /2 ML Co /Ir/Al_2O_3(0001) taken along the $\overline{\Gamma}$-$\overline{K}$ direction. Normalized spin-resolved EDCs (blue/red colors for spin up/down respectively) corresponding to (b) the in-plane chiral and (c) out-of-plane spin components, taken at the momentum position indicated by the orange vertical line in (a). Red and blue solid lines are fits to the experimental data. The in-plane spin projections are perpendicular to the momentum direction in (a). Individual peaks labelled according to the corresponding band features are displayed at the bottom of each panel. Measurements were taken at photon energy of hν=64 eV.

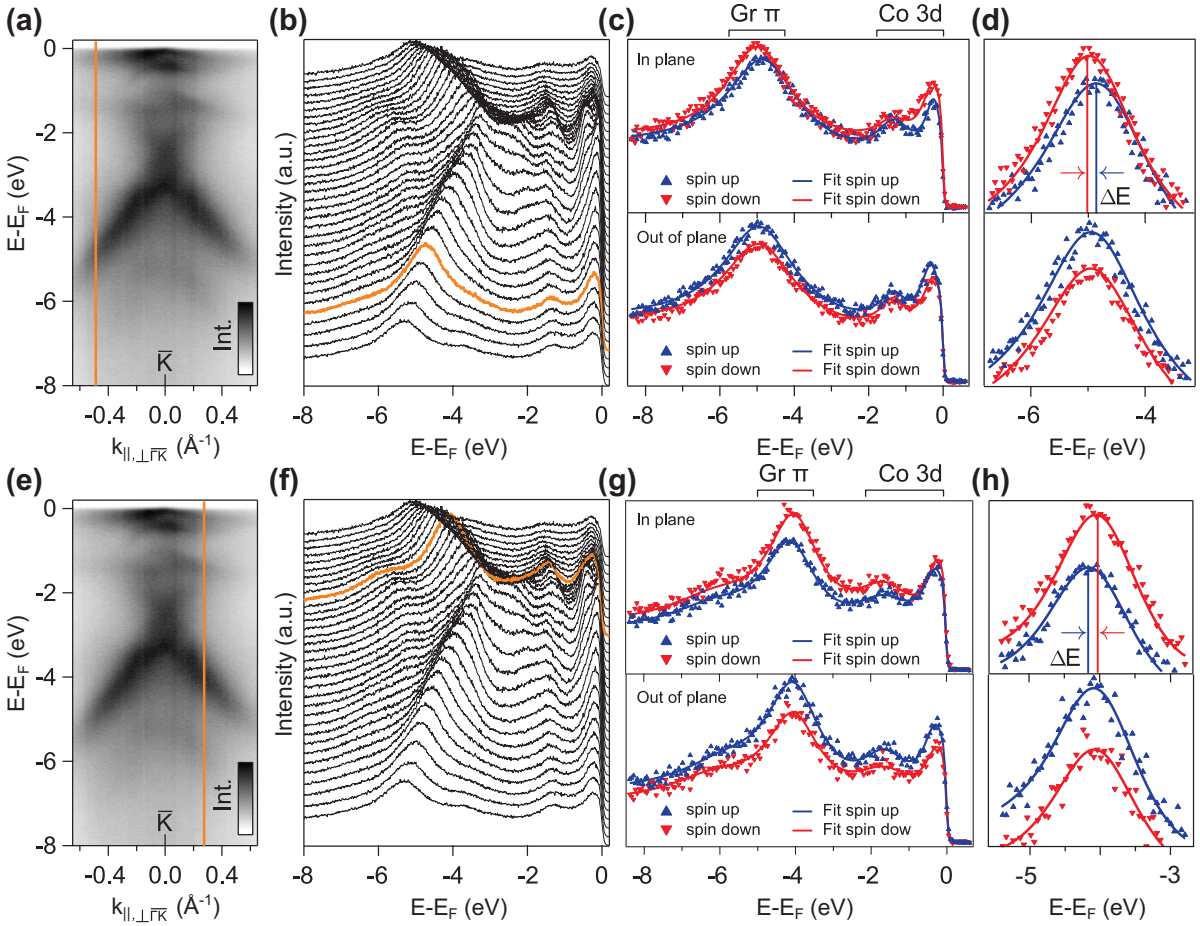

FIG. 6. **Rashba effect on Gr π states for 4 ML Co.** (a) ARPES band dispersion of Gr/4 ML Co/Ir(111) single-crystal centered at the $\overline{\text{K}}$ point along the momentum direction of the Gr SBZ orthogonal to $\overline{\Gamma}$-$\overline{\text{K}}$. (b) Evenly-spaced EDC profiles over the full momentum range shown in (a). (c),(d) Spin-resolved EDCs taken at the momentum position indicated by both the vertical solid line in (a) and the spin-integrated EDC highlighted in (b). The spin-resolved EDCs corresponding to the in-plane chiral (perpendicular to momentum direction in (a)) and out-of-plane spin components are shown in the top and bottom panels respectively. Solid lines are fits to the data (see Methods). (d) Zoom-in over the range of the Gr π band. The spin splitting of the in-plane channel (ΔE) is indicated. (e)-(h) ARPES and spin-resolved ARPES measurements analogous to those shown in (a)-(d) taken at opposite momentum with respect to $\overline{\text{K}}$. The observed reversal of the spin-orbit splitting in the in-plane chiral spin component is indicated in panel (h). Measurements were taken at photon energy of hν=45 eV.

tion from Gr π states, with the spin up and spin down components shown in blue and red color, respectively. Note that these were simultaneously acquired using independent electron counters.

As clearly seen in Fig. 5(b), there is a large energy spin-splitting in the in-plane chiral spin component for Gr π states of $\Delta E_{\text{in-plane}} \approx 100$ meV. In contrast, the out-of-plane spin up and down spectra do not show any sizeable spin splitting above the average error, as shown in Fig. 5(c). The energy spin splitting seen in the in-plane chiral spin component for the Gr π band is consistent in size with the one reported for Au and Pb intercalated layers at similar k values along the $\overline{\Gamma}$-$\overline{\text{K}}$ direction [33, 34].

This result is further corroborated in Fig. 6 with measurements for 4 ML Co intercalated Gr on an Ir(111) single crystal along the momentum direction of the Gr SBZ orthogonal to the $\overline{\Gamma}$-$\overline{\text{K}}$ direction. Note that similarly to Fig. 5, the in-plane chiral spin up and spin down orientations in Fig. 6 (which are perpendicular to the electron momentum), are also tangential to the Dirac cone, however rotated by 90° with respect to Fig. 5. Figures 6(a) and 6(b) provide a spin-integrated band dispersion of the Dirac cone alongside spin-integrated EDCs. Figure 6(c) shows spin-resolved EDCs corresponding to the in-plane chiral and out-of-plane spin components, measured at the momentum position indicated by the vertical line in Fig. 6(a), whose spin-integrated EDC is highlighted in Fig. 6(b). As seen in the zoom-in over the range corresponding to the Gr π band in Fig. 6(d), a large energy spin splitting of $\Delta E \approx 100$ meV, consistent with the spin-resolved measurements of Fig. 5, is clearly resolved in the in-plane chiral spin component for Gr π states. Figures 6(e)-(h) show ARPES and spin-resolved ARPES measurements corresponding to the ones shown in Figs. 6(a)-(d) but taken at opposite momentum with respect to $\overline{\text{K}}$, as indicated in Figs. 6(e),(f). A reversal of

the spin-orbit splitting in the in-plane chiral spin component is clearly observed and highlighted in Fig. 6(h).

Altogether, the chiral spin up and spin down orientations in Figs. 5(b) and 6(c) are consistent with a spin-orbit splitting predominantly associated with an in-plane Rashba-type spin texture, that is characterized by a counterclockwise (clockwise) spin circulation around $\overline{\mathrm{K}}$ for the outer (inner) π band spin states. First, the Rashba scenario is fully supported by the spin-resolved EDCs shown in Figs. 5(b) and 6(c), as both in-plane chiral spin components are tangential to the Dirac cone but rotated by 90° to each other. This observation rules out the possibility of a collinear alignment of antiparallel spin vectors in a global spin texture whose origin would be entirely magnetic. Second, the observed reversal of the spin-orbit splitting at opposite wave vectors confirms a Rashba effect. It should be noted that due to the energy dependent hybridization, spin-orbit effects with reducing energy are increasingly more difficult to resolve, as the lower half of the Dirac cone possesses very strong Co character, resulting in an overall spin texture that is more complex. This effect is manifested by an out-of-plane canting of electron spins which can be nevertheless observed in Figs. 6(d) and 6(h), despite the reduced Co weight in this energy region.

As a next step, spin-resolved ARPES measurements were performed on the thicker 10 ML Co system (see Fig. S5 in Supp. Info.), whose band dispersion is presented in Fig. 2(c). Despite the increasing spectral broadening of Gr π states induced by Co intercalation, any possible spin-orbit splitting of considerable size between opposite spin states is not observed. The absence of a measurable spin-orbit splitting for Gr π states in thicker intercalated Co films is in agreement with previous findings for Gr grown on 15 ML Co/W(110) [45]. W and Ir have similar spin-orbit coupling strength. These observations support our ARPES findings that at larger Co thickness the Gr/Co interface is electronically decoupled from the Ir layer, and emphasize the critical role of the interaction between Gr and the heavy metal layer via the FM as source of SOC for Gr atoms. The long range of the coupling across several atomic layers is also not unprecedented: Noble metal films on W(110) show a Rashba splitting [47]. For 1 to 7 ML thickness, it was shown that the Rashba splitting is the same for Au films and Ag films despite the very different size of the SOC. This shows that the SOC originates from the W substrate.

Hence, a large Rashba-SOC at the Gr/Co interface originating from the Gr layer, which in contrast to our findings was previously thought to be negligible [20] and thus not important for the observed enhancement of interfacial DMI, is consistent with the energy spin splitting observed in the in-plane chiral spin component for Gr π states in the thinner intercalated Co heterostructure.

DFT calculations of Co-intercalated Gr/Ir interface

To further verify our experimental findings, we performed DFT calculations for 2 ML of epitaxial Co intercalated at a Gr 1×1 /Ir(111) interface, with spin-orbit interaction fully taken into account. A complete description of the used procedures is included in the Methods section, and additional calculations are provided in Figs. S6 and S7 of the Supp. Info. To reduce the complexity of the problem, in the calculations Gr 1×1 was expanded to match with the Ir lattice, and thus $\overline{\mathrm{K}}$ and $\overline{\mathrm{M}}$ high-symmetry points are referred to the Ir(111) SBZ. In this way, contributions from the moiré superlattice of Gr to the electronic structure are explicitly neglected, although the spin splitting and the induced (in-plane) spin-polarization features are well considered. To give a comparison, a p(2×2) Gr relaxed on a $(\sqrt{3}\times\sqrt{3})$ Co/Ir(111) was calculated and the unfolded band structure (to the 1×1 Gr unit cell) is shown in Fig. S7. Compared to the p(1×1) structure, a slight difference in the doping level of the upper Dirac cone and a reduced splitting is noticed, but the discussed Gr bands between -5 and -8 eV along $\overline{\Gamma}$-$\overline{\mathrm{K}}$ are almost unaffected. In Fig. 7(a) the surface-projected band structure for Gr /2 ML Co /Ir(111) as determined by DFT along the $\overline{\Gamma}$-$\overline{\mathrm{K}}$-$\overline{\mathrm{M}}$-$\overline{\Gamma}$ direction is displayed. Here, the contribution of the k-resolved density of states (DOS) of Gr and Ir at the Gr/Co interface is highlighted, and the color representation indicates opposite orientations of the in-plane chiral spin component at the interface, which are perpendicular to electron momentum. The area of the circles is proportional to DOS (Gr) $\times$ DOS (Ir), being thus indicative of the hybridization between Gr and Ir. Overall, the calculation shows qualitatively good agreement with the experimental results.

By directly comparing the DFT calculations with the experiment, the preservation of the Gr π bands and their hybridization with Ir and Co-derived states at the interface is clear, resulting in a significant Gr-Ir interaction (region indicated with a rectangle in Fig. 7(a)). The main Dirac crossing point of the Gr π band at the $\overline{\mathrm{K}}$ point is located at an energy of E-$\mathrm{E_F}$ = -3 eV, in good agreement with the experimental results (see Fig. 2(b) and Figs. S1-S4 of the Supp. Info.). Similarly, in Fig. 7(a), clear signatures of the Gr-Ir hybridization can be also identified at -1.5 eV and in the vicinity of $\mathrm{E_F}$ around $\overline{\mathrm{K}}$ (horizontal black arrows), where the strong Co-Gr hybridization gives rise to the characteristic mini Dirac cone as experimentally observed (Fig. 4(c)). Note that the calculations neglect the band shift due to electron doping, and therefore the mini Dirac cone appears slightly above $\mathrm{E_F}$. Moreover, near the $\overline{\mathrm{M}}$ point there is a small enhancement of the DOS (horizontal black arrow in Fig. 7(a)) consistent with the Ir-Co hybridization that is observed in the ARPES measurements (Figs. 3, 4 and Fig. S3 in Supp. Info.).

In Fig. 7(b), a closer view of the energy-momentum dispersion of Gr π states along the $\overline{\Gamma}$-$\overline{\mathrm{K}}$ direction is provided, showing the calculated in-plane chiral spin component in the Gr layer within the energy and momentum ranges corresponding to the region indicated by a rectangle in Fig. 7(a). The chiral spin up and spin down orientations in Fig. 7(b) correspond to those in Fig. 7(a). There is a large energy spin splitting in the in-plane chiral spin component between Gr π states of opposite spin, confirming the crucial role of the spin-orbit interaction induced in the Gr layer for the enhancement of SOC

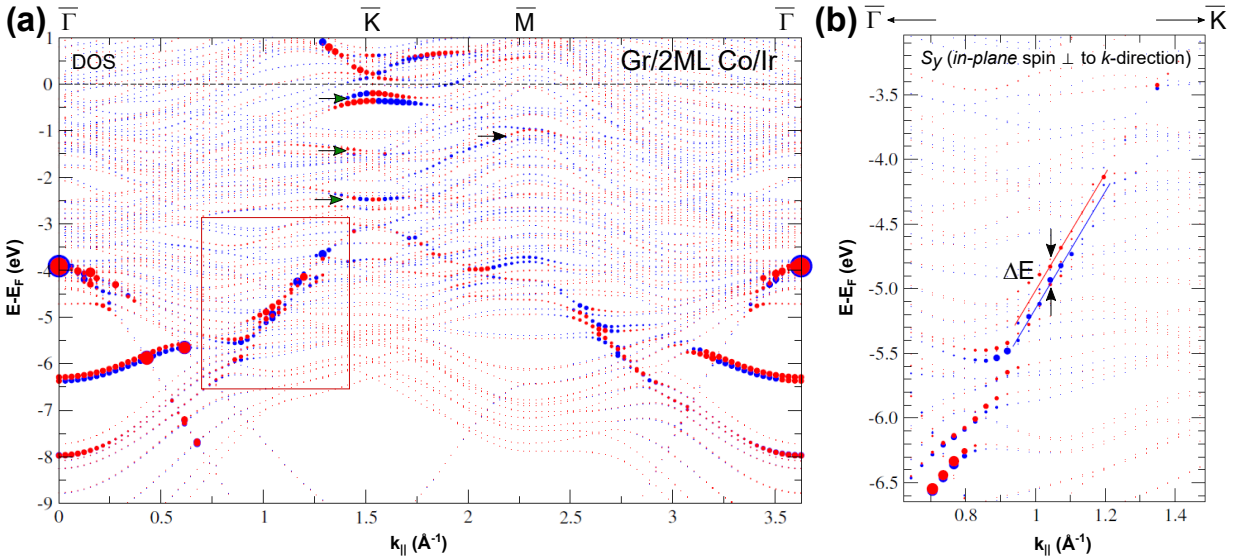

FIG. 7. **Theoretical prediction of Rashba effect on Gr on Ir through 2 ML Co.** (a) Surface-projected band structure of Gr /2 ML Co /Ir(111) as determined by DFT (see Methods) along the $\overline{\Gamma}$-$\overline{K}$-$\overline{M}$-$\overline{\Gamma}$ direction. The area of the circles is proportional to the product of the Gr and interface Ir DOS, while the color representation indicates the opposite orientations of the in-plane chiral spin component along the direction perpendicular to electron momentum. (b) Spin-resolved valence band structure corresponding to the calculated in-plane chiral spin orientations in the Gr layer. A close view of the energy-momentum dispersion of Gr π states along the $\overline{\Gamma}$-$\overline{K}$ direction is seen. The energy and momentum ranges correspond to the region of the Dirac cone with strong Gr character indicated by a rectangle in (a).

at the interface. The spin splitting is significantly pronounced in an energy region between -6 eV and -4 eV as the electron momentum approaches $\overline{K}$ point, in very good agreement with the spin-resolved ARPES measurements (Figs. 5 and 6). This spin-orbit splitting, which exceeds by far the one originating from SOC spatial variations in the Co layer and is highlighted by red and blue solid lines in Fig. 7(b), is in quantitative agreement with the energy spin splitting experimentally observed, that is, we recall, ≈ 100 meV. Consistent with this, a careful examination of the Gr π states in this energy region clearly shows that they are hybridized with the states localized at Ir (and Co) at the interface (larger DOS inside the rectangle in Fig. 7(a)). Thus, our theoretical calculations largely agree with the experimental results and demonstrate the strong electronic interaction between electronic states of Gr and those of the Ir-Co interface as well as a pronounced spin-orbit splitting. In other words, the obtained results confirm the Rashba-like spin-texture induced by Ir in the Gr layer and provide insight into the microscopic mechanism that is ultimately responsible for the significant enhancement of SOC at the Gr/Co interface that is experimentally discovered here.

Conclusions

To summarize, through ARPES with and without spin resolution in combination with DFT calculations we have investigated the electronic origin of the large DMI at Gr/FM interfaces. To this end, we have performed a systematic experimental characterization of the electronic properties of high-quality Gr-based heterostructures presenting atomically flat interfaces and homogeneous epitaxial Co layers intercalated between Gr and an Ir(111) layer and grown on insulating substrates. Our findings reveal that, in contrast to conventional wisdom, spin-orbit effects induced in the Gr layer are of central importance to fundamentally understand the enhancement of the SOC at Gr/FM interfaces. The effect is manifested by a large energy spin splitting in the in-plane chiral spin component for Gr π states, consistent with a Rashba spin texture and a spin-orbit splitting that exceeds by far the one originating from SOC variations in the Co layer. The experimental results are supported by DFT calculations pinpointing the interaction between Gr and the Ir layer as the main source of SOC for Gr atoms. The effect disappears with large separation from the Ir as demonstrated for 10 ML Co. These findings are consistent with a large Rashba-SOC at the Gr/Co interface arising from the Gr layer in ultrathin intercalated Co films, and are important towards achieving better control of the interfacial properties. We have demonstrated a convenient and very sensitive way of probing the SOC at the Gr-Co interface. This, and the demonstration that the interaction is mainly provided by the heavy metal layer, will help developing graphene-based memory and logic devices on insulating substrates.

Methods

Sample growth and characterization. The pristine, 2 ML Co and 10 ML Co samples were grown at the Molecular Beam Epitaxy (MBE) chamber at IMDEA Nanoscience (Madrid, Spain), and transferred to the Cassiopée beamline end station at the SOLEIL synchrotron light source (Gif-sur-Yvette, France) using an ultrahigh vacuum (UHV) suitcase at pressures below 5×10^{-10} mbar. Gr-based epitax-

ial heterostructures were grown under UHV conditions on commercially available Al_2O_3(0001)-oriented oxide single crystals. The insulating substrates were *ex-situ* annealed in air at 1370 K for 2 hours in order to obtain flat surfaces with large terraces prior to their insertion into the MBE chamber. Epitaxial (111)-oriented 30 nm thick Ir buffers were deposited by DC sputtering at 670 K in 8×10^{-3} mbar Ar partial pressure with a deposition rate of 0.3 Å/s. The epitaxial quality of the fabricated Ir layers was verified by LEED and XPS. Epitaxial Gr was subsequently grown at 1025 K by exposing the samples to ethylene gas at a partial pressure of 2×10^{-8} mbar for 30 min. After cooling down to room temperature, Co was deposited by electron-beam evaporation on top of Gr/Ir/Al_2O_3(0001) with a deposition rate of 0.04 Å/s, while its intercalation under Gr was promoted by a moderate thermal annealing. During this process, the sample was gradually heated up to 550 K while acquiring XPS spectra to verify in real time the complete intercalation of Co underneath the Gr layer. The XPS spectrum of Co was not modified by the presence of Co-C [64] which rules out diffusion of C. The 4 ML Co-intercalated sample for spin-resolved ARPES measurements was grown *in-situ* at the spin-ARPES end station permanently installed at the U125-2-PGM beamline of BESSY II. The Co source was carefully calibrated using a quartz crystal monitor.

Photoemission experiments. ARPES measurements were carried out at room temperature at the Cassiopée beamline HR-ARPES end station, and at the spin-ARPES end station at the U125-2-PGM beamline of of the synchrotron light source BESSY II in Helmholtz-Zentrum Berlin. Photoemission spectra were acquired using linearly-polarized light at photon energies of $h\nu = 64$ eV and 45 eV, respectively. The base pressures of the photoemission setups were better than 1×10^{-10} mbar. check previous version. Emitted photoelectrons were detected with Scienta R4000 hemispherical analyzers up to acceptance angles of $\pm15^\circ$. The angular and energy resolutions were set to 0.1° and 5 meV, respectively.

Spin-resolved measurements. Spin-resolved ARPES spectra in Fig. 5 were acquired at a photon energy of 64 eV at the spin-ARPES end station of Cassiopée beamline at SOLEIL synchrotron, using a SES2002 Scienta analyzer coupled to a Mini-Mott spin detector capable of detecting simultaneously both in-plane chiral (perpendicular to the analyzer horizontal entrance slit) and out-of-plane spin components (perpendicular to the surface plane). The energy resolution of the spin-resolved measurements was 230 meV, and the angular resolution was 3.6°. Spin-resolved ARPES measurements in Fig. 6 were taken at a photon energy of 45 eV at the U125-2-PGM beamline of the BESSY II synchrotron light source, using a Scienta R4000 analyzer (vertical entrance slit) coupled to a Rice University Mott-type spin polarimeter operated at 25 kV. The samples were measured in remanence after applying a pulsed magnetic field of 0.5 T under an angle of 45° with respect to the surface normal. Resolutions of the spin-resolved ARPES measurements were 45 meV (energy) and 0.75° (angular). The spin-resolved EDCs were fit using Lorentzian peaks and a Shirley background, multiplied with a Fermi function, and convoluted with a Gaussian broadening to account for the finite experimental resolution.

Theoretical calculations. We used DFT in the generalized gradient approximation [74] employing the full-potential linearized augmented-plane-wave method as implemented in the FLEUR code [75]. Relativistic effects, including spin-orbit coupling, were fully included. To calculate the electronic structure of Gr 1×1 /2 ML Co /Ir(111), a seven layer Ir(111) film was used as substrate, and different stackings were considered as a starting point for the structures to relax. The lowest energy was obtained when one C atom was situated above the top Co and the other in a fcc position. To obtain the surface- and spin-projected band structures, spin-orbit coupling with an out-of-plane spin-quantization axis was considered, enabling non-collinear calculations to resolve the in-plane spin components in the different layers.

Acknowledgements

This project has received funding from the FLAG-ERA JTC 2019 grant SOgraphMEM through the partner's national research agencies (Spain, AEI PCI2019-111867-2, France, ANR-19-GRF1-0001-07, Germany DFG-SOgraphMEM). IMDEA team acknowledges support from the Community of Madrid (CM) through Projects P2018/NMT-4321 (NANOMAGCOST) and MAD2D-CM-UAM funded by Comunidad de Madrid, the Spanish AEI/MICINN through Projects RTI2018-097895-B-C42 (FUN-SOC), PGC2018-098613-B-C21 (SpOrQuMat), PID2021-122980OB-C52 (ECLIPSE-ECoSOx), EQC2019-006304-P, PID2020-116181RB-C31 (SOnanoBRAIN), CNS2022-136143 (SPIN-CODE) and PID2021-123776NB-C21 (CONPHASE^{TM}), and from the 'Severo Ochoa' Programme for Centres of Excellence in R&D, MINECO grant CEX2020-001039-S. B.M.C., A.G. and I.A. acknowledge support from CM (PEJD-2019-PRE/IND-17048, PEJD-2017-PRE/IND-4690 and PEJD-2019-POST/IND-15343, respectively) and J.M.D. from MINECO (BES 2017-080617). The authors acknowledge the funding from the EMPIR Programme co-financed by the Participating States and the European and Union's Horizon 2020 Research and Innovation Programme (grant EMPIR 20FUN03 COMET), We acknowledge SOLEIL for provision of synchrotron radiation facilities and we would like to thank CASSIOPÉE beamline staff for assistance (experiment no. 20181593) and SEXTANTS beamline staff (in-house experiments). J.S.-B. acknowledges financial support from the Impuls- und Vernetzungsfonds der Helmholtz-Gemeinschaft under grant No. HRSF-0067. P.P. acknowledges fruitful discussions with Dr. Nicolas Jaouen, Dr. Jorge I. Cerdá (in memoriam) and Prof. Andrés Arnau.

Supporting information available

Additional ARPES experimental data and theoretical calculations are available online.

Associated Content

Beatriz Muñiz Cano, Adrián Gudín, Jaime Sánchez-Barriga, Oliver J. Clark, Alberto Anadón, Jose Manuel Díez, Pablo Olleros-Rodríguez, Fernando Ajejas, Iciar Arnay, Matteo Jugovac, Julien Rault, Patrick Le Fèvre, François Bertran, Donya Mazhjoo, Gustav Bihlmayer, Stefan Blügel, Rodolfo Miranda, Julio Camarero, Miguel Angel Valbuena, Paolo Perna. *Rashba-like spin textures in Graphene promoted by ferromagnet-mediated Electronic-Hybridization with heavy metal* (1 May 2023) arXiv:2206.04351v2 [cond-mat.mtrl-sci]. https://doi.org/10.48550/arXiv.2206.04351

References

† These authors contributed equally to this work.
* Authors to whom any correspondence should be addressed. E-mails: miguelangel.valbuena@imdea.org; paolo.perna@imdea.org

[1] K. Sato, E. Saitoh, A. Willoughby, P. Capper, and S. O. Kasap, *Spintronics for Next Generation*, 1st ed., Wiley Series in Materials for Electronic and Optoelectronic Applications (John Wiley Sons Inc, United Kingdom, 2015).

[2] A. H. Castro Neto, F. Guinea, N. M. R. Peres, K. S. Novoselov, and A. K. Geim, "The electronic properties of graphene," Rev. Mod. Phys. **81**, 109 (2009).

[3] W. Han, R. K. Kawakami, M. Gmitra, and J. Fabian, "Graphene spintronics," Nat. Nanotechnol. **9**, 794 (2014).

[4] A. Avsar, H. Ochoa, F. Guinea, B. Ozyilmaz, B. J. van Wees, and I. J. Vera-Marun, "Colloquium: Spintronics in graphene and other two-dimensional materials," Rev. Mod. Phys. **92**, 021003 (2020).

[5] M. Drögeler, C. Franzen, F. Volmer, T. Pohlmann, L. Banszerus, M. Wolter, K. Watanabe, T. Taniguchi, C. Stampfer, and B. Beschoten, "Spin lifetimes exceeding 12 ns in graphene nonlocal spin valve devices," Nano Lett. **16**, 3533–3539 (2016).

[6] M. H. Guimarães, P. J. Zomer, J. Ingla-Aynés, J. C. Brant, N. Tombros, and B. J. Van Wees, "Controlling spin relaxation in hexagonal BN-encapsulated graphene with a transverse electric field," Phys. Rev. Lett. **113**, 086602 (2014).

[7] J. Ingla-Aynés, M. H. D. Guimarães, R. J. Meijerink, P. J. Zomer, and B. J. van Wees, "24-μm spin relaxation length in boron nitride encapsulated bilayer graphene," Phys. Rev. B **92**, 201410 (2015).

[8] W. Yan, E. Sagasta, M. Ribeiro, Y. Niimi, L. E. Hueso, and F. Casanova, "Large room temperature spin-to-charge conversion signals in a few-layer graphene/Pt lateral heterostructure," Nat. Commun. **8**, 661 (2017).

[9] W. Savero Torres, J. F. Sierra, L. A. Benitez, F. Bonell, M. V. Costache, and S. O. Valenzuela, "Spin precession and spin Hall effect in monolayer graphene/Pt nanostructures," 2D Mater. **4**, 041008 (2017).

[10] A. Soumyanarayanan, N. Reyren, A. Fert, and C. Panagopoulos, "Emergent phenomena induced by spin-orbit coupling at surfaces and interfaces," Nature **539**, 509 (2016).

[11] C. L. Kane and E. J. Mele, "Quantum spin Hall effect in graphene," Phys. Rev. Lett. **95**, 226801 (2005).

[12] B. A. Bernevig, T. L. Hughes, and S.-C. Zhang, "Quantum spin Hall effect and topological phase transition in HgTe quantum wells," Science **314**, 1757–1761 (2006).

[13] M. König, S. Wiedmann, C. Brüne, A. Roth, H. Buhmann, L. W. Molenkamp, X. L. Qi, and S. C. Zhang, "Quantum spin Hall insulator state in HgTe quantum wells," Science **318**, 766–770 (2007).

[14] W. K. Tse, Z. Qiao, Y. Yao, A. H. MacDonald, and Q. Niu, "Quantum anomalous Hall effect in single-layer and bilayer graphene," Phys. Rev. B **83**, 155447 (2011).

[15] C. Weeks, J. Hu, J. Alicea, M. Franz, and R. Wu, "Engineering a robust quantum spin Hall state in graphene via adatom deposition," Phys. Rev. X **1**, 021001 (2011).

[16] H. Zhang, C. Lazo, S. Blügel, S. Heinze, and Y. Mokrousov, "Electrically tunable quantum anomalous Hall effect in graphene decorated by 5d transition-metal adatoms," Phys. Rev. Lett. **108**, 056802 (2012).

[17] C.-Z. Chang, J. Zhang, X. Feng, J. Shen, Z. Zhang, M. Guo, K. Li, Y. Ou, P. Wei, L.-L. Wang, Z.-Q. Ji, Y. Feng, S. Ji, X. Chen, J. Jia, X. Dai, Z. Fang, S.-C. Zhang, K. He, Y. Wang, L. Lu, X.-C. Ma, and Q.-K. Xue, "Experimental observation of the quantum anomalous Hall effect in a magnetic topological insulator," Science **340**, 167–170 (2013).

[18] I. Dzyaloshinsky, "A thermodynamic theory of "weak" ferromagnetism of antiferromagnetics," Journal of Physics and Chemistry of Solids **4**, 241–251 (1958).

[19] T. Moriya, "Anisotropic superexchange interaction and weak ferromagnetism," Phys. Rev. Journals Archive **120**, 91 (1960).

[20] H. Yang, G. Chen, A. A. C. Cotta, A. T. N'Diaye, S. A. Nikolaev, E. A. Soares, W. A. A. Macedo, K. Liu, A. K. Schmid, A. Fert, and M. Chshiev, "Significant Dzyaloshinskii–Moriya interaction at graphene–ferromagnet interfaces due to the Rashba effect," Nature Mater. **17**, 605–609 (2018).

[21] A. Hallal, J. Liang, F. Ibrahim, H. Yang, A. Fert, and M. Chshiev, "Rashba-type Dzyaloshinskii–Moriya interaction, perpendicular magnetic anisotropy, and skyrmion states at 2D materials/Co interfaces," Nano Lett. **21**, 7138–7144 (2021).

[22] A. Fert, V. Cros, and J. Sampaio, "Skyrmions on the track," Nat. Nanotechnol. **8**, 152–156 (2013).

[23] X. Z. Yu, Y. Onose, N. Kanazawa, J. H. Park, J. H. Han, Y. Matsui, N. Nagaosa, and Y. Tokura, "Real-space observation of a two-dimensional skyrmion crystal," Nature **465**, 901–904 (2010).

[24] K. Cai, M. Yang, H. Ju, S. Wang, Y. Ji, B. Li, K. W. Edmonds, Y. Sheng, B. Zhang, N. Zhang, S. Liu, H. Zheng, and K. Wang, "Electric field control of deterministic current-induced magnetization switching in a hybrid ferromagnetic/ferroelectric structure," Nature Materials **16**, 712–716 (2017).

[25] G. Yu, P. Upadhyaya, Y. Fan, J. G. Alzate, W. Jiang, K. L. Wong, S. Takei, S. A. Bender, L. T. Chang, Y. Jiang, M. Lang, J. Tang, Y. Wang, Y. Tserkovnyak, P. K. Amiri, and K. L. Wang, "Switching of perpendicular magnetization by spin–orbit torques in the absence of external magnetic fields," Nature Nanotechnology **9**, 548–554 (2014).

[26] Y. Cao, Y. Sheng, K. W. Edmonds, Y. Ji, H. Zheng, and K. Wang, "Deterministic magnetization switching using lateral spin–orbit torque," Advanced Materials **32**, 1907929 (2020).

[27] Y. Cao, X. Zhang, X. P. Zhang, F. Yan, Z. Wang, W. Zhu, H. Tan, V. N. Golovach, H. Zheng, and K. Wang, "Room-temperature van der Waals perpendicular ferromagnet through interlayer magnetic coupling," Physical Review Applied **17**, L051001 (2022).

[28] M. Gmitra, S. Konschuh, C. Ertler, C. Ambrosch-Draxl, and J. Fabian, "Band-structure topologies of graphene: spin-orbit

coupling effects from first principles," Phys. Rev. B **80**, 235431 (2009).

[29] D. Marchenko, J. Sánchez-Barriga, M. R. Scholz, O. Rader, and A. Varykhalov, "Spin splitting of Dirac fermions in aligned and rotated graphene on Ir(111)," Phys. Rev. B **87**, 115426 (2013).

[30] A. Avsar, J. Y. Tan, T. Taychatanapat, J. Balakrishnan, G. K. Koon, Y. Yeo, J. Lahiri, A. Carvalho, A. S. Rodin, E. C. O'Farrell, G. Eda, A. H. Castro Neto, and B. Özyilmaz, "Spin–orbit proximity effect in graphene," Nat. Commun. **5**, 4875 (2014).

[31] J. Balakrishnan, G. K. W. Koon, A. Avsar, Y. Ho, J. H. Lee, M. Jaiswal, S. J. Baeck, J. H. Ahn, A. Ferreira, M. A. Cazalilla, A. H. Neto, and B. Özyilmaz, "Giant spin effect in graphene grown by chemical vapour deposition," Nat. Commun. **5**, 4748 (2014).

[32] Y. S. Dedkov, M. Fonin, U. Rüdiger, and C. Laubschat, "Rashba effect in the graphene/Ni(111) system," Phys. Rev. Lett. **100**, 107602 (2008).

[33] D. Marchenko, A. Varykhalov, M. R. Scholz, G. Bihlmayer, E. I. Rashba, A. Rybkin, A. M. Shikin, and O. Rader, "Giant Rashba splitting in graphene due to hybridization with gold," Nat. Commun. **3**, 1232 (2012).

[34] M. M. Otrokov, I. I. Klimovskikh, F. Calleja, A. M. Shikin, O. Vilkov, A. G. Rybkin, D. Estyunin, S. Muff, J. H. Dil, A. L. Vázquez De Parga, R. Miranda, H. Ochoa, F. Guinea, J. I. Cerdá, E. V. Chulkov, and A. Arnau, "Evidence of large spin-orbit coupling effects in quasi-free-standing graphene on Pb/Ir(111)," 2D Mater. **5**, 035029 (2018).

[35] F. Calleja, H. Ochoa, M. Garnica, S. Barja, J. J. Navarro, A. Black, M. M. Otrokov, E. V. Chulkov, A. Arnau, A. L. Vázquez De Parga, F. Guinea, and R. Miranda, "Spatial variation of a giant spin–orbit effect induces electron confinement in graphene on Pb islands," Nat. Phys. **11**, 43–47 (2015).

[36] A. Varykhalov, J. Sánchez-Barriga, D. Marchenko, P. Hlawenka, P. S. Mandal, and O. Rader, "Tunable Fermi level and hedgehog spin texture in gapped graphene," Nat. Commun. **6**, 7610 (2015).

[37] I. I. Klimovskikh, O. Vilkov, D. Y. Usachov, A. G. Rybkin, S. S. Tsirkin, M. V. Filianina, K. Bokai, E. V. Chulkov, and A. M. Shikin, "Variation of the character of spin-orbit interaction by Pt intercalation underneath graphene on Ir(111)," Phys. Rev. B **92**, 165402 (2015).

[38] D. Marchenko, A. Varykhalov, J. Sánchez-Barriga, Th. Seyller, and O. Rader, "Rashba splitting of 100 mev in Au-intercalated graphene on SiC," Appl. Phys. Lett. **108**, 172405 (2016).

[39] I. I. Klimovskikh, M. M. Otrokov, V. Y. Voroshnin, D. Sostina, L. Petaccia, G. Di Santo, S. Thakur, E. V. Chulkov, and A. M. Shikin, "Spin–orbit coupling induced gap in graphene on Pt(111) with intercalated Pb monolayer," ACS Nano **11**, 368 (2017).

[40] V. M. Karpan, G. Giovannetti, P. A. Khomyakov, M. Talanana, A. A. Starikov, M. Zwierzycki, J. V. D. Brink, G. Brocks, and P. J. Kelly, "Graphite and graphene as perfect spin filters," Phys. Rev. Lett. **99**, 176602 (2007).

[41] M. Piquemal-Banci, R. Galceran, S. M. Dubois, V. Zatko, M. Galbiati, F. Godel, M. B. Martin, R. S. Weatherup, F. Petroff, A. Fert, J. C. Charlier, J. Robertson, S. Hofmann, B. Dlubak, and P. Seneor, "Spin filtering by proximity effects at hybridized interfaces in spin-valves with 2D graphene barriers," Nat. Commun. **11**, 5670 (2020).

[42] A. Anadón, A. Gudín, R. Guerrero, I. Arnay, A. Guedeja-Marron, P. Jiménez-Cavero, J. M. Díez Toledano, F. Ajejas, M. Varela, S. Petit-Watelot, I. Lucas, L. Morellón, P. A. Algarabel, M. R. Ibarra, R. Miranda, J. Camarero, J. C. Rojas-Sánchez, and P. Perna, "Engineering the spin conversion in graphene monolayer epitaxial structures," APL Materials **9**, 061113 (2021).

[43] P. Gargiani, R. Cuadrado, H. B. Vasili, M. Pruneda, and M. Valvidares, "Graphene-based synthetic antiferromagnets and ferrimagnets," Nat. Commun. **8**, 699 (2017).

[44] E. Cobas, A. L. Friedman, O. M. J. van't Erve, J. T. Robinson, and B. T. Jonker, "Graphene as a tunnel barrier: graphene-based magnetic tunnel junctions," Nano Lett. **12**, 3000–3004 (2012).

[45] O. Rader, A. Varykhalov, J. Sánchez-Barriga, D. Marchenko, A. Rybkin, and A. M. Shikin, "Is there a Rashba effect in graphene on 3d ferromagnets?" Phys. Rev. Lett. **102**, 057602 (2009).

[46] A. Varykhalov, J. Sánchez-Barriga, A. M. Shikin, C. Biswas, E. Vescovo, A. Rybkin, D. Marchenko, and O. Rader, "Electronic and magnetic properties of quasifreestanding graphene on Ni," Phys. Rev. Lett. **101**, 157601 (2008).

[47] A. Varykhalov, J. Sánchez-Barriga, A. M. Shikin, W. Gudat, W. Eberhardt, and O. Rader, "Quantum cavity for spin due to spin-orbit interaction at a metal boundary," Phys. Rev. Lett. **101**, 256601 (2008).

[48] P. Moras, G. Bihlmayer, P. M. Sheverdyaeva, S. K. Mahatha, M. Papagno, J. Sánchez-Barriga, O. Rader, L. Novinec, S. Gardonio, and C. Carbone, "Magnetization-dependent Rashba splitting of quantum well states at the Co/W interface," Phys. Rev. B **91**, 195410 (2015).

[49] M. Jugovac, I. Cojocariu, J. Sánchez-Barriga, P. Gargiani, M. Valvidares, V. Feyer, S. Blügel, G. Bihlmayer, and P. Perna, "Inducing single spin-polarized flat bands in monolayer graphene," Adv. Mater. **35**, 2301441 (2023).

[50] N. Rougemaille, A. T. Ndiaye, J. Coraux, C. Vo-Van, O. Fruchart, and A. K. Schmid, "Perpendicular magnetic anisotropy of cobalt films intercalated under graphene," Appl. Phys. Lett. **101**, 142403 (2012).

[51] M. Blanco-Rey, P. Perna, A. Gudin, J. M. Diez, A. Anadón, P. Olleros-Rodríguez, L. de Melo Costa, M. Valvidares, P. Gargiani, A. Guedeja-Marron, M. Cabero, M. Varela, C. García-Fernández, M. M. Otrokov, J. Camarero, R. Miranda, A. Arnau, and J. I. Cerdá, "Large perpendicular magnetic anisotropy in nanometer-thick epitaxial graphene/Co/heavy metal heterostructures for spin–orbitronics devices," ACS Appl. Nano Mater. **4**, 4398–4408 (2021).

[52] H. Yang, A. D. Vu, A. Hallal, N. Rougemaille, J. Coraux, A. K. Schmid, and M. Chshiev, "Anatomy and giant enhancement of the perpendicular magnetic anisotropy of cobalt–graphene heterostructures," Nano Lett. **16**, 145–151 (2015).

[53] F. Ajejas, A. Gudin, R. Guerrero, A. Anadón, J. M. Diez, L. D. M. Costa, P. Olleros, M. A. Niño, S. Pizzini, J. Vogel, M. Valvidares, P. Gargiani, M. Cabero, M. Varela, J. Camarero, R. Miranda, and P. Perna, "Unraveling Dzyaloshinskii–Moriya interaction and chiral nature of graphene/cobalt interface," Nano Lett. **18**, 5364–5372 (2018).

[54] C. Vo-Van, Z. Kassir-Bodon, Y. Hongxin, J. Coraux, J. Vogel, S. Pizzini, P. Bayle-Guillemaud, M. Chrhiev, L. Ranno, and V. Guisset, "Ultrathin epitaxial cobalt films on graphene for spintronic investigations and applications," New J. Phys. **12**, 103040 (2010).

[55] P. Olleros-Rodríguez, R. Guerrero, J. Camarero, O. Chubykalo-Fesenko, and P. Perna, "Intrinsic mixed Bloch–Néel character and chirality of skyrmions in asymmetric epitaxial trilayers," ACS Appl. Mater. Interfaces **12**, 25419–25427 (2020).

[56] Y. Wang, L. Wang, J. Xia, Z. Lai, G. Tian, X. Zhang, Z. Hou, X. Gao, W. Mi, C. Feng, M. Zeng, G. Zhou, G. Yu, G. Wu,

Y. Zhou, W. Wang, X. Zhang, and J. Liu, "Electric-field-driven non-volatile multi-state switching of individual skyrmions in a multiferroic heterostructure," Nat. Commun. **11**, 3577 (2020).

[57] D. Usachov, A. Fedorov, M. M. Otrokov, A. Chikina, O. Vilkov, A. Petukhov, A. G. Rybkin, Y. M. Koroteev, E. V. Chulkov, V. K. Adamchuk, A. Gru, C. Laubschat, and D. V. Vyalikh, "Observation of single-spin Dirac fermions at the graphene/ferromagnet interface," Nano Lett. **15**, 2396–2401 (2015).

[58] D. Pacilé, S. Lisi, I. Di Bernardo, M. Papagno, L. Ferrari, M. Pisarra, M. Caputo, S. K. Mahatha, P. M. Sheverdyaeva, P. Moras, P. Lacovig, S. Lizzit, A. Baraldi, M. G. Betti, and C. Carbone, "Electronic structure of graphene/Co interfaces," Phys. Rev. B **90**, 195446 (2014).

[59] H. Vita, S. Böttcher, P. Leicht, K. Horn, A. B. Shick, and F. Máca, "Electronic structure and magnetic properties of cobalt intercalated in graphene on Ir(111)," Phys. Rev. B **90**, 165432 (2014).

[60] M. Jugovac, F. Genuzio, T. O. Mentes, A. Locatelli, G. Zamborlini, V. Feyer, and C. M. Schneider, "Tunable coupling by means of oxygen intercalation and removal at the strongly interacting graphene/cobalt interface," Carbon **163**, 341–347 (2020).

[61] A. Fert and P. M. Levy, "Role of anisotropic exchange interactions in determining the properties of spin-glasses," Phys. Rev. Lett. **44**, 1538 (1980).

[62] AR Fert, "Magnetic and transport properties of metallic multilayers," in *Materials science forum*, Vol. 59 (Trans Tech Publ, 1990) pp. 439–480.

[63] M. Blanco-Rey, G. Bihlmayer, A. Arnau, and J. I. Cerda, "Nature of interfacial Dzyaloshinskii-Moriya interactions in graphene/Co/Pt (111) multilayer heterostructures," Phys. Rev. B **106**, 064426 (2022).

[64] F. Ajejas, A. Anadon, A. Gudin, J. M. Diez, C. G. Ayani, P. Olleros-Rodríguez, L. De Melo Costa, C. Navío, A. Gutierrez, F. Calleja, A. L. Vázquez De Parga, R. Miranda, J. Camarero, and P. Perna, "Thermally activated processes for ferromagnet intercalation in graphene-heavy metal interfaces," ACS Appl. Mater. Interfaces, **12**, 4088–4096 (2019).

[65] A. Anadón, A. Gudin, R. Guerrero, I. Arnay, A. Guedeja-Marron, P. Jiménez-Cavero, J. M. Diez Toledano, F. Ajejas, M. Varela, S. Petit-Watelot, I. Lucas, L. Morellón, P. A. Algarabel, M. R. Ibarra, R. Miranda, J. Camarero, and J. C. Rojas-Sánchez, "Engineering the spin conversion in graphene monolayer epitaxial structures," APL Mater. **9**, 061113 (2021).

[66] I. Pletikosic, M. Kralj, P. Pervan, R. Brako, J. Coraux, A. T. N. Diaye, C. Busse, and T. Michely, "Dirac cones and minigaps for graphene on Ir(111)," Phys. Rev. Lett. **102**, 056808 (2009).

[67] M. Kralj, I. Pletikosić, M. Petrović, P. Pervan, M. Milun, A. T. N. Diaye, C. Busse, T. Michely, J. Fujii, and I. Vobornik, "Graphene on Ir(111) characterized by angle-resolved photoemission," Phys. Rev. B **84**, 075427 (2011).

[68] I. Pletikosic, M. Kralj, D. Sokcevic, R. Brako, P. Lazic, and P. Pervan, "Photoemission and density functional theory study of Ir(111): energy band gap mapping," J. Phys.: Condens. Matter **22**, 135006 (2010).

[69] E. Starodub, A. Bostwick, L. Moreschini, S. Nie, F. E. Gabaly, K. F. McCarty, and E. Rotenberg, "In-plane orientation effects on the electronic structure, stability, and Raman scattering of monolayer graphene on Ir(111)," Phys. Rev. B **83**, 125428 (2011).

[70] A. T. N. N'Diaye, J. Coraux, T. N. Plasa, C. Busse, and T. Michely, "Structure of epitaxial graphene on Ir(111)," New J. Phys. **10**, 043033 (2008).

[71] A. Varykhalov, D. Marchenko, M. R. Scholz, E. D. Rienks, T. K. Kim, G. Bihlmayer, J. Sánchez-Barriga, and O. Rader, "Ir(111) surface state with giant Rashba splitting persists under graphene in air," Phys. Rev. Lett. **108**, 066804 (2012).

[72] P. Zhang, P. Richard, T. Qian, Y. Xu, X. Dai, and H. Ding, "A precise method for visualizing dispersive features in image plots," Rev. Sci. Instrum. **82**, 043712 (2011).

[73] K. Wang, T. Vincent, J.B. Bouhiron, S. Pons, D. Roditchev, S. Simon, M. Fonin, B. Paulus, Y. Dedkov, S. Vlaic, and E. Voloshina, "Influence of surface and subsurface Co–Ir alloy on the electronic properties of graphene," Carbon **183**, 251–258 (2021).

[74] J. P. Perdew, K. Burke, and M. Ernzerhof, "Generalized gradient approximation made simple," Phys. Rev. Lett. **77**, 3865 (1996).

[75] P. Kurz, F. Förster, L. Nordström, G. Bihlmayer, and S. Blügel, "*Ab initio* treatment of noncollinear magnets with the full-potential linearized augmented plane wave method," Phys. Rev. B **69**, 024415 (2004).

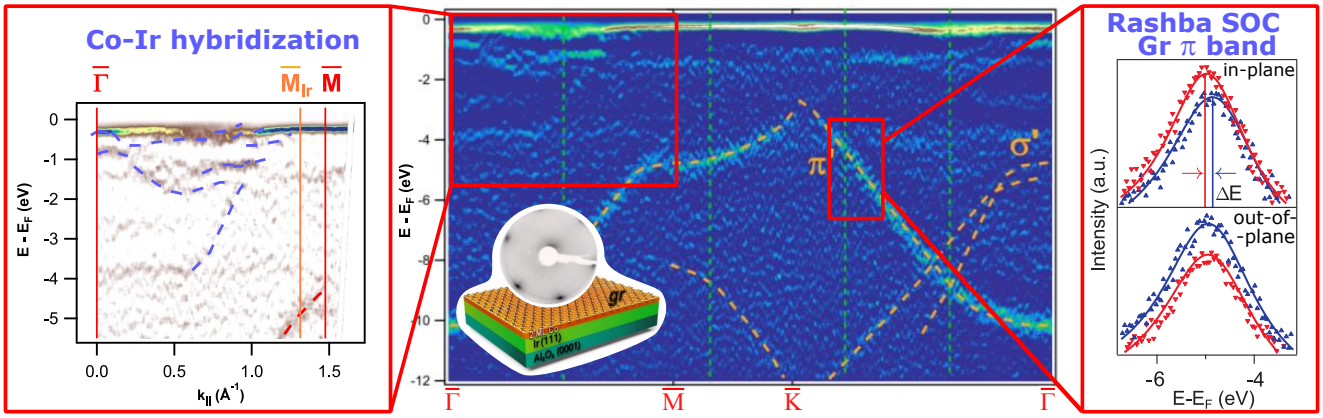

For Table of Contents Only